Available online at www.sciencedirect.com
SCIENCE DIRECT
Polymer 47 (2006) 3616–3628
polymer
www.elsevier.com/locate/polymer

Small-angle X-ray scattering of long-period structures forming bundles

Masatoshi Shioya [a,*], Tomomi Kawazoe [a], Junichi Kojima [b], Shinichi Sakurai [c], Katsuhiro Yamamoto [d], Takeshi Kikutani [a]

[a] *Department of Organic and Polymeric Materials, Tokyo Institute of Technology, S8-34, 2-12-1 O-okayama, Meguro-ku, Tokyo 152-8552, Japan*
[b] *Japan Chemical Innovation Institute, 3-29-8 Kitasenzoku, O-taku, Tokyo 145-0062, Japan*
[c] *Department of Polymer Science and Engineering, Kyoto Institute of Technology, Matsugasaki, Sakyo-ku, Kyoto 606-8585, Japan*
[d] *Graduate School of Engineering, Nagoya Institute of Technology, Gokiso-cho, Showa-ku, Nagoya 466-8555, Japan*

Received 23 June 2005; received in revised form 27 December 2005; accepted 17 March 2006

Abstract

Small-angle X-ray scattering (SAXS) patterns have been calculated based on a structure model, which consisted of the bundles of long-period structures. The proposed model has produced various scattering patterns of polymers, such as the equatorial, layer line, four-spot, droplet-shaped and triangular scattering. The 0.5th order scattering has arisen when the disorder in or between the long-period structures was large even though the structure did not have the periodicity directly related to the scattering maximum. A slight decrease in the disorder due to slip between the long-period structures has accounted for the sudden change of the SAXS pattern of a poly(ethylene terephthalate) fiber from the four-spot to the layer line scattering which was caused by a slight tensile deformation.

Keywords: Small-angle X-ray scattering; Poly(ethylene terephthalate) fiber; Tensile deformation

1. Introduction

Poly(ethylene terephthalate) (PET) fibers and films produce widely varying small-angle X-ray scattering (SAXS) patterns depending on the processing conditions, the degree of deformation and the temperature of measurement. The melt-spun PET fibers produce, depending on the take-up speed, the equatorial streak, the cross-shaped scattering and the triangular scattering with its apex on the center of the scattering pattern [1–4]. The drawn and annealed PET fibers produce the four-spot scattering [2]. The PET bristles [5] and films [6] produce the layer line scattering, which is a striation parallel to the equator and intersecting the meridian of the scattering pattern. Most of these scatterings arise from the electron density difference between the amorphous and the crystalline regions that compose the long-period structure and the difference in the arrangements of these regions gives rise to the variation of the scattering patterns.

The present authors have measured SAXS of a single filament of PET during tensile deformation using synchrotron radiation. The incident X-ray beam was perpendicular to the fiber axis. The tensile strain and stress applied to the fiber when the scattering patterns were measured and those values at fiber break are shown in Table 1. Before deformation, the PET fiber produced the four-spot scattering as shown in the inset of Fig. 1. By applying a slight deformation, this scattering was rapidly changed into the layer line scattering. The intensity distributions of the PET fiber under deformation which were measured along the line U–V in Fig. 2 are shown in Fig. 1 by the dots. The intensity distributions were markedly changed by a slight increase in deformation in a manner that the scattering intensity increased mainly around the meridian. Similar change of the scattering pattern has been observed during tensile deformation of the PET films [6]. Why the layer line scattering was not accompanied by the equatorial streak and why the four-spot scattering was changed into the layer line scattering by the application of such a small deformation are the main concerns of the present study.

An isolated long-period structure produces a series of scattering spots. The smaller the transverse size of the long-period structure is, the wider the scattering spots are in the same direction. Therefore, the layer line scattering can be produced by a long-period structure with a small transverse size. In this case, however, the zeroth order (central) scattering spot is also wide and the equatorial streak is to be produced. The SAXS patterns showing the layer line scattering without

* Corresponding author. Tel./fax: +81 3 5734 2434.
E-mail address: mshioya@o.cc.titech.ac.jp (M. Shioya).

0032-3861/$ - see front matter © 2006 Elsevier Ltd. All rights reserved.
doi:10.1016/j.polymer.2006.03.063

Table 1
Tensile strain and stress applied to a PET fiber, those values at fiber break and values of sin γ $|\mathbf{u}_1|$ and $|\mathbf{u}_3|$

Strain	Stress (GPa)	sin γ $\lvert\mathbf{u}_1\rvert$ (nm)	$\lvert\mathbf{u}_3\rvert$ (nm)
0	0	5.39	13.8
0.01	0.10	5.24	13.8
0.02	0.16	5.20	13.7
0.03	0.20	4.99	14.3
0.04	0.27	5.05	14.5
0.48	0.96	Fiber break	

the equatorial streak have been calculated based on an isolated long-period structure model by Tsvankin et al. [7–10]. They have used, however, an interference function in which the zeroth order peak has not been incorporated (i.e. the case of $|A_1|=1$ has been excluded from Eq. (4) of Ref. [7]) and the equatorial streak would have arisen if this term had been appropriately incorporated.

Stockfleth et al. [6] have attributed the layer line scattering without the equatorial streak to the long-period structures having inclined interfaces between amorphous and crystalline regions. A long-period structure having inclined interfaces produces scattering spots off the longitudinal direction. They have regarded the layer line scattering as an assembly of many scattering spots that were produced by the long-period structures having various inclinations of the interfaces. For the scattering spots to lie on a layer line, the inclinations of the interfaces have to be widely distributed but the periods have to be constant for all the long-period structures. Based on this model, they have explained the change of the scattering pattern caused by tensile deformation similar to Fig. 1. They have

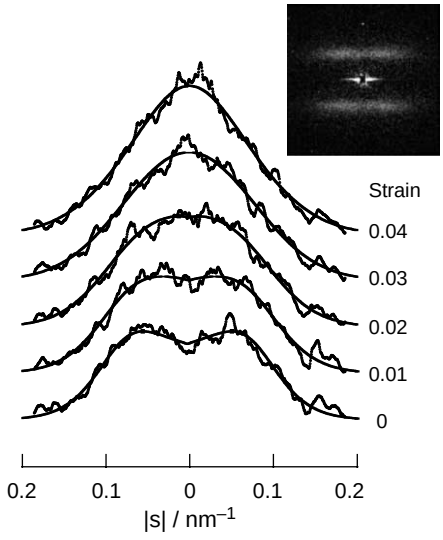

Fig. 1. Dots indicate measured SAXS intensity distributions of a PET fiber at various strains shown in the figure. Intensity distributions were measured along the line U–V shown in Fig. 2 that passed through the intensity maximum. Intensity distributions were shifted vertically in order to avoid overlap. Solid lines indicate calculated intensity distributions based on F11 with the values of the structure parameters shown in Tables 1 and 3 and Fig. 9. Inset is SAXS pattern of the PET fiber at a strain of 0. Fiber axis is vertical. Incident X-ray beam was perpendicular to the fiber axis.

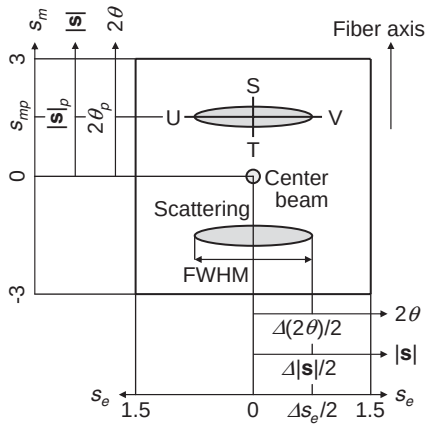

Fig. 2. Schematic illustration of scattering patterns.

attributed the increase in the scattering intensity around the longitudinal direction (i.e. the meridian for the fibers and the loading axis for the films) to the decrease in the electron density of the amorphous regions in the long-period structures that had small inclinations of the interfaces. For the scattering to be kept on the layer line, the periods of all the long-period structures should be increased consistently during tensile deformation.

In the present study, the layer line scattering without the equatorial streak will be attributed to the bundle of long-period structures, which are arranged with a disorder. The change of the scattering pattern from the four-spot to the layer line scattering will be attributed to the decrease in the disorder. The outline of this paper is as follows. Firstly, the scattering intensity will be derived based on the structure model, which consists of the bundle of long-period structures. Secondly, a couple of equations for determining the structure parameters from the intensity distributions will be derived. Thirdly, the scattering patterns of the structure model will be calculated using various values of the structure parameters. It will be demonstrated that the proposed structure model produces not only the layer line and the four-spot scattering but also the equatorial, the triangular and the droplet-shaped [9] scattering. It will be also demonstrated that the 0.5th order scattering arises when the disorder is large. Lastly, the intensity distributions shown in Fig. 1 will be analyzed based on the proposed structure model. The equations, which will be derived in this study, can also be applied to neutron scattering if the intensity I_e of X-ray scattered by the electron will be replaced with the intensity of neutron scattered by the atom.

2. Theoretical

2.1. Structure model and definitions

In this study, SAXS caused by the electron density difference between amorphous and crystalline regions is considered. It is assumed that a pair of adjacent amorphous and crystalline regions composes a unit cell, the unit cells are arranged in one direction forming a rod and the rods are aligned

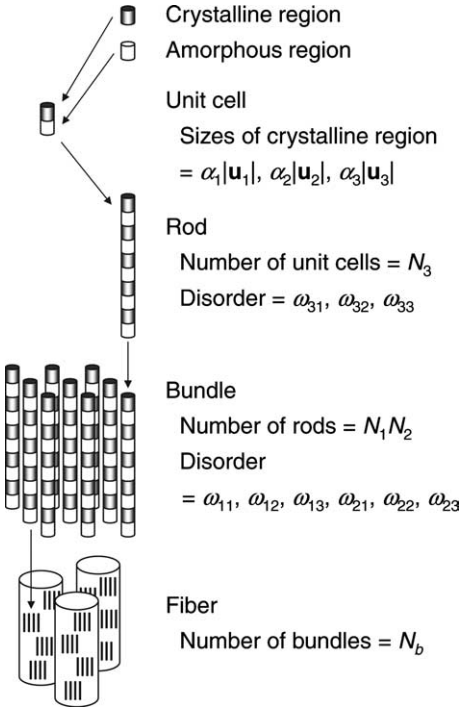

Fig. 3. Structure model consisting of the bundles of long-period structures.

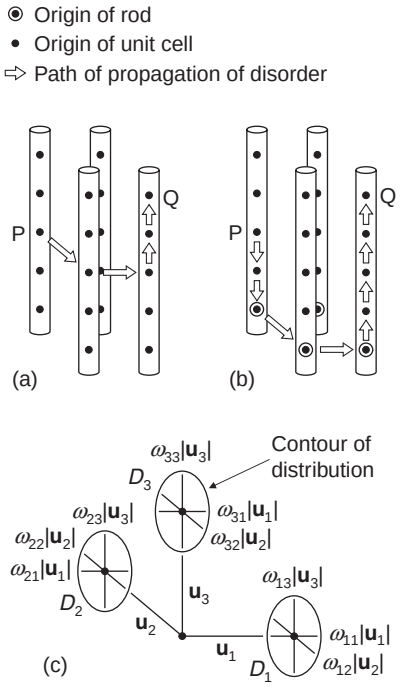

Fig. 4. Arrows indicate paths from starting unit cell P to ending unit cell Q, which are followed in calculating convolution products for (a) three- and (b) one-dimensionally propagating disorder. Contours of function D_j are schematically illustrated in (c).

in parallel with each other forming a bundle (Fig. 3). Such bundles are dispersed in the irradiated volume of the specimen without interference of X-rays.

It is assumed that the arrangement of the unit cells is disturbed with the disorder of the second kind [11]. If the disorder is of the first kind, the unit cells are displaced stochastically in reference to the regular lattice points. If the disorder is of the second kind, on the other hand, the unit cells are displaced stochastically in reference to the positions of the neighbouring unit cells. In this case, the distribution of the vectors joining two unit cells gets broader as the number of the unit cells separating those two unit calls increases. This broadening of the distribution with increasing separation will be called propagation of disorder and can be represented by the convolution product of distribution functions. If the distribution of the vectors from the unit cells to the neighbouring unit cells is represented by a certain distribution function, the vectors from the neighbouring unit cells to the second neighbouring unit cells also distribute according to the same distribution function. Therefore, the vectors joining the unit cells and the second neighbouring unit cells distribute according to the convolution product of the same two distribution functions. Similarly, the distribution of the vectors joining the unit cells, which are farther apart is obtained by performing the convolution product of a number of distribution functions following the path from the starting to the ending unit cell. With the present structure model, several different paths can be drawn between two unit cells in the bundle. If some interaction has worked between the unit cells in neighbouring rods during forming process of the structure, spatial correlation exists between the unit cells in neighbouring rods. In this case, the convolution product is performed following the path shown in Fig. 4(a). This type of disorder will be called three-dimensionally propagating disorder. If, on the other hand, the arrangement of the unit cells in the rod has been developed without any interaction between the unit cells in neighbouring rods, the arrangements of the unit cells in different rods are independent. There are spatial correlations between the unit cells in the same rod and between the rods in a bundle. In this case, the convolution product is performed following the path shown in Fig. 4(b). This type of disorder will be called one-dimensionally propagating disorder. With respect to the two-dimensional arrangement of the origins of the rods in a bundle, two- and one-dimensionally propagating disorder can be considered in a similar way.

The following notations will be used in this study (Figs. 2–4).

$\mathbf{u}_3$	average period between unit cells along a rod.
$\mathbf{u}_1, \mathbf{u}_2$	average periods between rods in a bundle.
γ	angle between $\mathbf{u}_1$ and $\mathbf{u}_2$.
v	volume of parallelepiped having edge vectors $\mathbf{u}_1$, $\mathbf{u}_2$ and $\mathbf{u}_3$.
$\mathbf{u}_1^*, \mathbf{u}_2^*, \mathbf{u}_3^*$	reciprocal vectors of $\mathbf{u}_1$, $\mathbf{u}_2$ and $\mathbf{u}_3$, respectively.
$\alpha_1\|\mathbf{u}_1\|, \alpha_2\|\mathbf{u}_2\|, \alpha_3\|\mathbf{u}_3\|$	sizes of crystalline region.
N_3	number of unit cells in a rod.
N_1, N_2	number of rods in a bundle counted in parallel to $\mathbf{u}_1$ and $\mathbf{u}_2$, respectively.
N_b	number of bundles in irradiated volume.

$D_j(\mathbf{x})$ distribution, around average period $\mathbf{u}_j$, of vectors $\mathbf{x}$ joining nearest neighbouring unit cells.
$\omega_{jk}|\mathbf{u}_k|$ distribution width or full-width at half-maximum (FWHM) of D_j in parallel to $\mathbf{u}_k$.
R_j, ζ_j absolute value and phase factor of Fourier transform of D_j, respectively.
ρ_d electron density difference between amorphous and crystalline region.
$\rho_u(\mathbf{x})$ electron density distribution in a unit cell where $\mathbf{x}$ issues from origin of unit cell.
$\rho_b(\mathbf{x})$ electron density distribution in a bundle where $\mathbf{x}$ issues from origin of bundle.
$I_e(\mathbf{s})$, $I_b(\mathbf{s})$, $I_s(\mathbf{s})$ scattering intensity by electron, bundle and irradiated volume, respectively.
$\mathbf{x}$ real space vector.
x_1, x_2, x_3 components of $\mathbf{x}$ with respect to base vectors $\mathbf{u}_1$, $\mathbf{u}_2$ and $\mathbf{u}_3$, respectively.
2θ scattering angle in radian.
$\mathbf{s}$ reciprocal space vector (scattering vector).
s_1, s_2, s_3 components of $\mathbf{s}$ with respect to base vectors $\mathbf{u}_1^*$, $\mathbf{u}_2^*$, and $\mathbf{u}_3^*$, respectively.
s_e, s_m components of $\mathbf{s}$ with respect to base vectors $\mathbf{u}_{12}^*$ and $\mathbf{u}_3^*$ as defined by Eq. (38). These components correspond to the equatorial and the meridional coordinate of fiber scattering patterns when the incident X-ray beam is perpendicular to the fiber axis.
$2\theta_p$, $|\mathbf{s}|_p$, s_{mp} peak positions of meridional scattering measured in parallel to meridian.
$\Delta(2\theta)$, $\Delta|\mathbf{s}|$, Δs_e FWHM's of meridional scattering measured in parallel to equator.
h_j integer closest to $s_j-\zeta_j$ representing order of scattering.
j, k indices showing directions of 1, 2 and 3.
λ X-ray wavelength.

The multiple convolution product is defined as

$$f(\mathbf{x})^{*n} = \begin{cases} \delta(\mathbf{x}) & (n=0) \\ [f(\mathbf{x})^{*n-1}]^* f(\mathbf{x}) & (n \geq 1) \end{cases} \tag{1}$$

where $f(x)^*g(x)$ stands for the convolution product of functions $f(x)$ and $g(x)$, and $\delta(\mathbf{x})$ is the three-dimensional Dirac delta function. The Fourier transforms of the functions of x_j and $\mathbf{x}$ are defined as:

$$F(f(x_j)) = \int_{-\infty}^{\infty} f(x_j)\exp(-2\pi i x_j s_j)\mathrm{d}x_j \tag{2}$$

$$F(f(\mathbf{x})) = \int_{-\infty}^{\infty}\int_{-\infty}^{\infty}\int_{-\infty}^{\infty} f(\mathbf{x})\exp(-2\pi i[x_1 s_1 + x_2 s_2 + x_3 s_3])v\mathrm{d}x_1\mathrm{d}x_2\mathrm{d}x_3 \tag{3}$$

The scattering vector is related to the scattering angle as:

$$|\mathbf{s}| = \frac{2}{\lambda}\sin\theta \tag{4}$$

Other fundamental relations, which will be used in this study have been summarized in Appendix of a paper treating X-ray diffraction of layer-type molecules [12].

2.2. Three-dimensionally propagating disorder

The scattering intensity of the bundle, I_b, is given by:

$$I_b(\mathbf{s}) = I_e(\mathbf{s})|F(\rho_b(\mathbf{x}))|^2 = I_e(\mathbf{s})F(\rho_b(-\mathbf{x})^*\rho_b(\mathbf{x})) \tag{5}$$

The following vectors are defined by numbering the unit cells and the rods.

$\mathbf{x}_r$ vector from origin of a bundle to origin of the rth rod in this bundle.
$\mathbf{x}_{rc}$ vector from origin of the rth rod to the cth unit cell in this rod.

The position of the cth unit cell in reference to the origin of the bundle can be represented by a distribution function $\delta(\mathbf{x}-[\mathbf{x}_r+\mathbf{x}_{rc}])$. The electron density distribution in a bundle is represented as:

$$\rho_b(\mathbf{x}) = \rho_u(\mathbf{x})^* \sum_{r=1}^{N_1N_2}\sum_{c=1}^{N_3}\delta(\mathbf{x}-[\mathbf{x}_r+\mathbf{x}_{rc}]) \tag{6}$$

The auto-correlation of ρ_b can be rearranged as:

$$\rho_b(-\mathbf{x})^*\rho_b(\mathbf{x}) = [\rho_u(-\mathbf{x})^*\rho_u(\mathbf{x})]^* \sum_{r,r'=1}^{N_1N_2}\sum_{c,c'=1}^{N_3} \times\delta(\mathbf{x}-[\mathbf{x}_r+\mathbf{x}_{rc}-\mathbf{x}_{r'}-\mathbf{x}_{r'c'}]) \tag{7}$$

The vector $\mathbf{x}_r+\mathbf{x}_{rc}-\mathbf{x}_{r'}-\mathbf{x}_{r'c'}$ joins the cth unit cell in the rth rod and the c'th unit cell in the r'th rod. For a regular lattice, $\Sigma\Sigma\delta(\mathbf{x}-[\mathbf{x}_r+\mathbf{x}_{rc}-\mathbf{x}_{r'}-\mathbf{x}_{r'c'}])$ shows discrete spikes at $\mathbf{x}=\mathbf{x}_r+\mathbf{x}_{rc}-\mathbf{x}_{r'}-\mathbf{x}_{r'c'}$ whereas for a disordered lattice, it shows broad peaks. In the latter case, the peak height decreases with increasing $|\mathbf{x}|$ since the number of the vectors joining two unit cells decreases with increasing $|\mathbf{x}|$ for the lattice with a finite size. The number of the vectors joining two unit cells is given by $Z_1(x_1)Z_2(x_2)Z_3(x_3)$ where:

$$Z_j(x_j) = \begin{cases} N_j - |x_j| & (|x_j| \leq N_j) \\ 0 & (\text{otherwise}) \end{cases} \tag{8}$$

Therefore, $\Sigma\Sigma\delta(\mathbf{x}-[\mathbf{x}_r+\mathbf{x}_{rc}-\mathbf{x}_{r'}-\mathbf{x}_{r'c'}])$ is given by the product of the number $Z_1(x_1)Z_2(x_2)Z_3(x_3)$ and the number average distribution of the vectors joining two unit cells in an

infinitely large lattice, $\langle\Sigma\Sigma\delta(\mathbf{x}-[\mathbf{x}_r+\mathbf{x}_{rc}-\mathbf{x}_{r'}-\mathbf{x}_{r'c'}])\rangle_Z$.

$$\rho_b(-\mathbf{x})^*\rho_b(\mathbf{x}) = [\rho_u(-\mathbf{x})^*\rho_u(\mathbf{x})]^*\left[Z_1(x_1)Z_2(x_2)Z_3(x_3) \times\left\langle\sum_{r,r'=-\infty}^{\infty}\sum_{c,c'=-\infty}^{\infty}\delta(\mathbf{x}-[\mathbf{x}_r+\mathbf{x}_{rc}-\mathbf{x}_{r'}-\mathbf{x}_{r'c'}])\right\rangle_Z\right] \tag{9}$$

It is assumed that the arrangement of the unit cells is disturbed with the three-dimensionally propagating disorder. The distribution of the vectors joining the nearest neighbouring unit cells can be represented as either $D_j(\mathbf{x}-\mathbf{u}_j)=D_j(\mathbf{x})*\delta(\mathbf{x}-\mathbf{u}_j)$ or $D_j(-\mathbf{x}-\mathbf{u}_j)=D_j(-\mathbf{x})*\delta(\mathbf{x}+\mathbf{u}_j)$ where $D_j(\mathbf{x})$ and $D_j(-\mathbf{x})$ are the distribution of $\mathbf{x}$ around the average periods $\mathbf{u}_j$ and $-\mathbf{u}_j$, respectively. The vectors joining the unit cells and their second neighbors in the direction of $\mathbf{u}_j$ distribute according to $D_j(\mathbf{x}-\mathbf{u}_j)*D_j(\mathbf{x}-\mathbf{u}_j)$. The vectors joining the unit cells and their neighbors in the direction of $\mathbf{u}_j+\mathbf{u}_k$ distribute according to $D_j(\mathbf{x}-\mathbf{u}_j)*D_k(\mathbf{x}-\mathbf{u}_k)$. By considering all the possible combinations of the starting and the ending unit cell, $\langle\Sigma\Sigma\delta(\mathbf{x}-[\mathbf{x}_r+\mathbf{x}_{rc}-\mathbf{x}_{r'}-\mathbf{x}_{r'c'}])\rangle_Z$ is represented as:

$$\begin{aligned}&\left\langle\sum_{r,r'=-\infty}^{\infty}\sum_{c,c'=-\infty}^{\infty}\delta(\mathbf{x}-[\mathbf{x}_r+\mathbf{x}_{rc}-\mathbf{x}_{r'}-\mathbf{x}_{r'c'}])\right\rangle_Z\\ &=\left[\sum_{n=1}^{\infty}D_1(-\mathbf{x}-\mathbf{u}_1)^{*n}+\delta(\mathbf{x})+\sum_{n=1}^{\infty}D_1(\mathbf{x}-\mathbf{u}_1)^{*n}\right]\\ &\quad*\left[\sum_{n=1}^{\infty}D_2(-\mathbf{x}-\mathbf{u}_2)^{*n}+\delta(\mathbf{x})+\sum_{n=1}^{\infty}D_2(\mathbf{x}-\mathbf{u}_2)^{*n}\right]\\ &\quad*\left[\sum_{n=1}^{\infty}D_3(-\mathbf{x}-\mathbf{u}_3)^{*n}+\delta(\mathbf{x})+\sum_{n=1}^{\infty}D_3(\mathbf{x}-\mathbf{u}_3)^{*n}\right]\end{aligned} \tag{10}$$

The Fourier transform of D_j is expressed using R_j and ζ_j as:

$$F(D_j(\mathbf{x})) = R_j\exp(2\pi i\zeta_j)\quad(0\le R_j\le 1 \text{ and } 0\le\zeta_j<1) \tag{11}$$

The Fourier transform of the convolution product of two functions is given by the product of the Fourier transforms of these functions. Ignoring the variations of R_j and ζ_j with s_j around each scattering peak, the following equation is derived.

$$\begin{aligned}F(\rho_b(-\mathbf{x})^*\rho_b(\mathbf{x})) &= |F(\rho_u(\mathbf{x}))|^2\\ &\times\left[F(Z_1(x_1))^*\sum_{n=-\infty}^{\infty}R_1^{|n|}\exp(2\pi in[s_1-\zeta_1])\right]\\ &\times\left[F(Z_2(x_2))^*\sum_{n=-\infty}^{\infty}R_2^{|n|}\exp(2\pi in[s_2-\zeta_2])\right]\\ &\times\left[F(Z_3(x_3))^*\sum_{n=-\infty}^{\infty}R_3^{|n|}\exp(2\pi in[s_3-\varsigma_3])\right]\end{aligned} \tag{12}$$

In the right side of this equation, the Fourier transforms and the convolution products are carried out with respect to x_j and s_j that appear in each line, respectively. The scattering intensity of the bundle with the three-dimensionally propagating disorder is finally derived as:

$$\begin{aligned}I_b(\mathbf{s}) &= I_e(\mathbf{s})|F(\rho_u(\mathbf{x}))|^2G(N_1,R_1,\zeta_1,s_1)\\ &\quad\times G(N_2,R_2,\zeta_2,s_2)G(N_3,R_3,\zeta_3,s_3)\end{aligned} \tag{13}$$

The function G is defined as (Appendix A)

$$\begin{aligned}G(N_j,R_j,\zeta_j,s_j) &= F(Z_j(x_j))^*\sum_{n=-\infty}^{\infty}R_j^{|n|}\exp(2\pi in[s_j-\zeta_j])\\ &=\frac{4R_jN_j^2}{(1+R_j)\left[(1-R_j)^2N_j^2+4\right]^{1/2}}\exp\left[-\frac{4\pi N_j^2(s_j-\varsigma_j-h_j)^2}{(1-R_j)^2N_j^2+4}\right]\\ &\quad+\frac{(1-R_j)N_j}{1+R_j}\end{aligned} \tag{14}$$

where the convolution product is carried out with respect to s_j. In the case of $N_j=1$, the exact value of $G=1$ should be used in order to reduce error. In the case of $R_j=0$, $G=N_j$ irrespective of s_j. In the case of $R_j>0$ and $N_j>1$, G produces peaks at $s_j=h_j+\zeta_j$ where the integer h_j represents the order of scattering. The peak intensity increases with increasing R_j. Eq. (13) indicates that the scattering intensity distribution of the bundle is given by the product of three functions, which determine the intensity distributions in the individual directions.

2.3. One-dimensionally propagating disorder

It is assumed that the arrangement of the unit cells is disturbed with the one-dimensionally propagating disorder and the arrangement of the origins of the rods is disturbed with the two-dimensionally propagating disorder. Eq. (7) can be rearranged as:

$$\begin{aligned}\rho_b(-\mathbf{x})^*\rho_b(\mathbf{x}) &= [\rho_u(-\mathbf{x})^*\rho_u(\mathbf{x})]\\ &*\left[\sum_{r,r'=1}^{N_1N_2}\sum_{c=1}^{N_3}\delta(\mathbf{x}-\mathbf{x}_{rc})^*\sum_{c'=1}^{N_3}\delta(\mathbf{x}+\mathbf{x}_{r'c'})^*\delta(\mathbf{x}-\mathbf{x}_r+\mathbf{x}_{r'})\right]\end{aligned} \tag{15}$$

Since the arrangements of the unit cells in different rods are independent, $\Sigma\delta(\mathbf{x}-\mathbf{x}_{rc})$ is independent of $\Sigma\delta(\mathbf{x}+\mathbf{x}_{r'c'})$ and $\delta(\mathbf{x}-\mathbf{x}_r+\mathbf{x}_{r'})$ if r is different from r'. Therefore, $\Sigma\delta(\mathbf{x}-\mathbf{x}_{rc})$ can be replaced by its average for all the rods, $\langle\Sigma\delta(\mathbf{x}-\mathbf{x}_{rc})\rangle_r$. Similarly, $\Sigma\delta(\mathbf{x}+\mathbf{x}_{r'c'})$ can be replaced by its average. The auto-correlation of ρ_b is rearranged as:

$$\begin{aligned}\rho_b(-\mathbf{x})^*\rho_b(\mathbf{x}) &= [\rho_u(-\mathbf{x})^*\rho_u(\mathbf{x})]\\ &*\left[\left\langle\sum_{c=1}^{N_3}\delta(\mathbf{x}-\mathbf{x}_{rc})\right\rangle_r^*\left\langle\sum_{c=1}^{N_3}\delta(\mathbf{x}+\mathbf{x}_{rc})\right\rangle_r^*\sum_{r,r'=1}^{N_1N_2}\delta(\mathbf{x}-\mathbf{x}_r+\mathbf{x}_{r'})\right.\\ &\quad-N_1N_2\left\langle\sum_{c=1}^{N_3}\delta(\mathbf{x}-\mathbf{x}_{rc})\right\rangle_r^*\left\langle\sum_{c=1}^{N_3}\delta(\mathbf{x}+\mathbf{x}_{rc})\right\rangle_r\\ &\quad\left.+\sum_{r=1}^{N_1N_2}\sum_{c,c'=1}^{N_3}\delta(\mathbf{x}-\mathbf{x}_{rc}+\mathbf{x}_{rc'})\right]\end{aligned} \tag{16}$$

The origins of unit cells that locate at the ends of rods are taken to be the origins of rods. The distribution of the vectors joining neighbouring unit cells in a rod is represented by D_3. The distribution of the vectors joining the origins of neighbouring rods is represented by D_1 and D_2. Each factor in Eq. (16) is represented as follows.

$$\left\langle \sum_{c=1}^{N_3} \delta(\mathbf{x}-\mathbf{x}_{rc}) \right\rangle_r = \sum_{n=0}^{N_3-1} D_3(\mathbf{x}-\mathbf{u}_3)^{*n} \tag{17}$$

$$\sum_{c,c'=1}^{N_3} \delta(\mathbf{x}-\mathbf{x}_{rc}+\mathbf{x}_{rc'}) = Z_3(x_3)\left\langle \sum_{c,c'=-\infty}^{\infty} \delta(\mathbf{x}-\mathbf{x}_{rc}+\mathbf{x}_{rc'}) \right\rangle_Z \tag{18}$$

$$\sum_{r,r'=1}^{N_1N_2} \delta(\mathbf{x}-\mathbf{x}_{r}+\mathbf{x}_{r'}) = Z_1(x_1)Z_2(x_2)\left\langle \sum_{r,r'=-\infty}^{\infty} \delta(\mathbf{x}-\mathbf{x}_{r}+\mathbf{x}_{r'}) \right\rangle_Z \tag{19}$$

where

$$\left\langle \sum_{c,c'=-\infty}^{\infty} \delta(\mathbf{x}-\mathbf{x}_{rc}+\mathbf{x}_{rc'}) \right\rangle_Z = \sum_{n=1}^{\infty} D_3(-\mathbf{x}-\mathbf{u}_3)^{*n} + \delta(\mathbf{x}) + \sum_{n=1}^{\infty} D_3(\mathbf{x}-\mathbf{u}_3)^{*n} \tag{20}$$

$$\left\langle \sum_{r,r'=-\infty}^{\infty} \delta(\mathbf{x}-\mathbf{x}_{r}+\mathbf{x}_{r'}) \right\rangle_Z = \left[\sum_{n=1}^{\infty} D_1(-\mathbf{x}-\mathbf{u}_1)^{*n} + \delta(\mathbf{x}) + \sum_{n=1}^{\infty} D_1(\mathbf{x}-\mathbf{u}_1)^{*n}\right] * \left[\sum_{n=1}^{\infty} D_2(-\mathbf{x}-\mathbf{u}_2)^{*n} + \delta(\mathbf{x}) + \sum_{n=1}^{\infty} D_2(\mathbf{x}-\mathbf{u}_2)^{*n}\right] \tag{21}$$

By performing the Fourier transform, the following equations are derived.

$$F(\rho_b(-\mathbf{x})^*\rho_b(\mathbf{x})) = |F(\rho_u(\mathbf{x}))|^2 \left[\left|F\left(\left\langle \sum_{c=1}^{N_3} \delta(\mathbf{x}-\mathbf{x}_{rc}) \right\rangle_r\right)\right|^2 F\left(\sum_{r,r'=1}^{N_1N_2} \delta(\mathbf{x}-\mathbf{x}_{r}+\mathbf{x}_{r'})\right) - N_1N_2\left|F\left(\left\langle \sum_{c=1}^{N_3} \delta(\mathbf{x}-\mathbf{x}_{rc}) \right\rangle_r\right)\right|^2 + \sum_{r=1}^{N_1N_2} F\left(\sum_{c,c'=1}^{N_3} \delta(\mathbf{x}-\mathbf{x}_{rc}+\mathbf{x}_{rc'})\right)\right] \tag{22}$$

$$\left|F\left(\left\langle \sum_{c=1}^{N_3} \delta(\mathbf{x}-\mathbf{x}_{rc}) \right\rangle_r\right)\right|^2 = \left|\sum_{n=0}^{N_3-1} R_3^n exp(2\pi ni[s_3-\zeta_3])\right|^2 \tag{23}$$

$$F\left(\sum_{c,c'=1}^{N_3} \delta(\mathbf{x}-\mathbf{x}_{rc}+\mathbf{x}_{rc'})\right) = F(Z_3(x_3))^* \sum_{n=-\infty}^{\infty} R_3^{|n|}\exp(2\pi ni[s_3-\zeta_3]) \tag{24}$$

$$F\left(\sum_{r,r'=1}^{N_1N_2} \delta(\mathbf{x}-\mathbf{x}_{r}+\mathbf{x}_{r'})\right) = \left[F(Z_1(x_1))^* \sum_{n=-\infty}^{\infty} R_1^{|n|}\exp(2\pi ni[s_1-\zeta_1])\right] \times \left[F(Z_2(x_2))^* \sum_{n=-\infty}^{\infty} R_2^{|n|}\exp(2\pi ni[s_2-\zeta_2])\right] \tag{25}$$

In the right sides of Eqs. (24) and (25), the Fourier transforms and the convolution products are carried out with respect to x_j and s_j that appear in each line, respectively. The scattering intensity of the bundle with the one-dimensionally propagating disorder is finally derived as:

$$I_b(\mathbf{s}) = I_e(\mathbf{s})|F(\rho_u(\mathbf{x}))|^2 \times [G(N_1,R_1,\varsigma_1,s_1)G(N_2,R_2,\varsigma_2,s_2)H(N_3,R_3,\varsigma_3,s_3) - N_1N_2H(N_3,R_3,\varsigma_3,s_3) + N_1N_2G(N_3,R_3,\varsigma_3,s_3)] \tag{26}$$

The functions H is defined as (Appendix A):

$$H(N_j,R_j,\varsigma_j,s_j) = \left|\sum_{n=0}^{N_j-1} R_j^n \exp(2\pi ni[s_j-\varsigma_j])\right|^2 = \frac{\left(1-R_j^{N_j}\right)^2 + 4R_j^{N_j}\sin^2(\pi N_j[s_j-\varsigma_j])}{(1-R_j)^2 + 4R_j\sin^2(\pi[s_j-\varsigma_j])} \tag{27}$$

In the case of $N_j=1$, the exact value of $H=1$ should be used in order to reduce error. It is known by comparing Eq. (26) with (13) that the scattering intensity for the one-dimensionally propagating disorder is obtained by replacing the function G that determines the intensity distribution in parallel to s_3 for the three-dimensionally propagating disorder by H and adding a factor in proportion to the difference between G and H.

2.4. Factors depending on degree of disorder

The parameter ζ_j has an important influence on the appearance of the scattering pattern since the 0.5th order scattering arises when $\zeta_j=1/2$. For an even function D_j, $F(D_j)$ takes a real number and ζ_j is either 0 or 1/2 depending on whether $F(D_j)$ is positive or negative at a given scattering angle, respectively.

When the vectors joining the nearest neighboring unit cells distribute uniformly in a certain volume, D_j can be represented

by a rectangular function as follows.

$$D_j(\mathbf{x}) = \begin{cases} \dfrac{1}{v\omega_{j1}\omega_{j2}\omega_{j3}} & \begin{pmatrix} (-\omega_{j1}/2) \le x_1 \le (\omega_{j1}/2) \\ (-\omega_{j2}/2) \le x_2 \le (\omega_{j2}/2) \\ (-\omega_{j3}/2) \le x_3 \le (\omega_{j3}/2) \end{pmatrix} \\ 0 & \text{(otherwise)} \end{cases} \tag{28}$$

where $j=1$, 2 or 3. The Fourier transform of this function is as follows.

$$R_j exp(2\pi i \varsigma_j) = \frac{\sin(\pi\omega_{j1}s_1)}{\pi\omega_{j1}s_1}\frac{\sin(\pi\omega_{j2}s_2)}{\pi\omega_{j2}s_2}\frac{\sin(\pi\omega_{j3}s_3)}{\pi\omega_{j3}s_3} \tag{29}$$

With the one-dimensionally propagating disorder, D_1 and D_2 represent the distributions of the vectors joining the origins of neighboring rods. In this case, the rods do not overlap with each other even though these functions have a long tail in parallel to $\mathbf{u}_3$. Therefore, the following distribution function can be used for D_1 and D_2.

$$D_j(\mathbf{x}) = \begin{cases} \left(\dfrac{\ln 2}{\pi}\right)^{1/2} \dfrac{2}{v\omega_{j1}\omega_{j2}\omega_{j3}} \exp\left(-4\ln 2\dfrac{x_3^2}{\omega_{j3}^2}\right) & \begin{pmatrix} (-\omega_{j1}/2) \le x_1 \le (\omega_{j1}/2) \\ (-\omega_{j2}/2) \le x_2 \le (\omega_{j2}/2) \end{pmatrix} \\ 0 & \text{(otherwise)} \end{cases} \tag{30}$$

where $j=1$ or 2. The FWHM of this distribution in parallel to $\mathbf{u}_3$ is $\omega_{j3}|\mathbf{u}_3|$. The Fourier transform of this function is as follows.

$$R_j \exp(2\pi i \varsigma_j) = \frac{\sin(\pi\omega_{j1}s_1)}{\pi\omega_{j1}s_1}\frac{\sin(\pi\omega_{j2}s_2)}{\pi\omega_{j2}s_2}\exp\left(-\frac{[\pi\omega_{j3}s_3]^2}{4\ln 2}\right) \tag{31}$$

The values of ω_{jk} should be chosen so as to avoid the overlap of unit cells. The conditions to avoid the overlap of the nearest neighboring unit cells are as follows. For the three-dimensionally propagating disorder:

$$\alpha_j + \frac{1}{2}\omega_{jj} \le 1 \tag{32}$$

For the one-dimensionally propagating disorder, by considering that the arrangements of the unit cells in neighboring rods are independent and hence the overlap of the unit cells locating at the ends of neighboring rods should be avoided:

$$\begin{cases} \alpha_j + \dfrac{1}{2}\omega_{jj} + (N_3 - 1)\omega_{3j} \le 1 & (j = 1 \text{ or } 2) \\ \alpha_j + \dfrac{1}{2}\omega_{jj} \le 1 & (j = 3) \end{cases} \tag{33}$$

2.5. Factor depending on unit cell shape

The factor $|F(\rho_u)|^2$ depends on the electron density distribution and the shape of the unit cell. By applying the Babinet principle, the electron density of the unit cell can be expressed as:

$$\rho_u(\mathbf{x}) = \begin{cases} \rho_d & \text{(in crystalline region)} \\ 0 & \text{(in amorphous region)} \end{cases} \tag{34}$$

By considering a parallelepiped-shaped unit cell, it is assumed that the crystalline region has the edge vectors $\alpha_1\mathbf{u}_1 + \beta_3\mathbf{u}_3$, $\alpha_2\mathbf{u}_2$, and $\alpha_3\mathbf{u}_3$. The parameter β_3 represents the inclination of the interface between the amorphous and the crystalline region. The factor $|F(\rho_u)|^2$ for the parallelepiped-shaped unit cell can be derived as:

$$\begin{aligned} |F(\rho_u(\mathbf{x}))|^2 &= (\rho_d\alpha_1\alpha_2\alpha_3 v)^2 \frac{\sin^2(\pi[\alpha_1 s_1 + \beta_3 s_3])}{(\pi[\alpha_1 s_1 + \beta_3 s_3])^2} \\ &\quad \times \frac{\sin^2(\pi\alpha_2 s_2)}{(\pi\alpha_2 s_2)^2}\frac{\sin^2(\pi\alpha_3 s_3)}{(\pi\alpha_3 s_3)^2} \\ &\approx (\rho_d\alpha_1\alpha_2\alpha_3 v)^2 \exp(-\pi[\alpha_1 s_1 + \beta_3 s_3]^2 \\ &\quad - \pi[\alpha_2 s_2]^2 - \pi[\alpha_3 s_3]^2) \end{aligned} \tag{35}$$

By considering a columnar unit cell, it is assumed that the two bases of the crystalline region are circular with a diameter $\alpha_1|\mathbf{u}_1| = \alpha_1|\mathbf{u}_2|$, centered at $(x_1, x_2, x_3) = (0, 0, 0)$ and $(0, 0, \alpha_3)$, and parallel to the plane including $\mathbf{u}_1$ and $\mathbf{u}_2$. For simplicity, it is assumed that $|\mathbf{u}_1| = |\mathbf{u}_2|$. The factor $|F(\rho_u)|^2$ for the columnar unit cell can be derived as:

$$\begin{aligned} |F(\rho_u(\mathbf{x}))|^2 &= \left(\frac{\pi\rho_d\alpha_1^2\alpha_3 v}{4\sin\gamma}\right)^2 \left(\frac{2J_1(Q)}{Q}\right)^2 \frac{\sin^2(\pi\alpha_3 s_3)}{(\pi\alpha_3 s_3)^2} \\ &\approx \left(\frac{\pi\rho_d\alpha_1^2\alpha_3 v}{4\sin\gamma}\right)^2 \exp(-0.2653Q^2)\exp(-\pi[\alpha_3 s_3]^2) \end{aligned} \tag{36}$$

$$Q = \frac{\pi\alpha_1}{\sin\gamma}\left(s_1^2 + s_2^2 - 2s_1 s_2 \cos\gamma\right)^{1/2} \tag{37}$$

The function J_n is the Bessel function of the first kind of order n. Both $(2J_1(Q)/Q)^2$ and its approximation $\exp(-0.2653Q^2)$ are 1 at $Q=0$ and the difference between the values of these functions is less than 0.04.

2.6. Scattering intensity of irradiated volume

The scattering intensity of the irradiated volume is given by the sum of the intensities of individual bundles since there is no interference of X-rays between the bundles. A coordinate rotation should be carried out according to the orientation distribution of the bundles before summing up the intensities of the bundles. The calculation procedure for the fiber system in which $\mathbf{u}_3$ of the bundles distributes around the fiber axis by keeping a cylindrical symmetry is similar to that shown in a previous paper [12]. In the present study, it is assumed that $\mathbf{u}_3$ of the bundles is in parallel to the fiber axis and $\mathbf{u}_1$ and $\mathbf{u}_2$

distribute around the fiber axis with a cylindrical symmetry. For simplicity, it is also assumed that $|\mathbf{u}_1|=|\mathbf{u}_2|$ and $\mathbf{u}_1$ and $\mathbf{u}_2$ are perpendicular to $\mathbf{u}_3$. In this case, $|\mathbf{u}_1^*|=|\mathbf{u}_2^*|=1/(|\mathbf{u}_1|\sin\gamma)$, $|\mathbf{u}_3^*|=1/|\mathbf{u}_3|$, $\mathbf{u}_1^*$ and $\mathbf{u}_2^*$ are perpendicular to $\mathbf{u}_3$, and $\mathbf{u}_3^*$ is parallel to $\mathbf{u}_3$. A radial vector $\mathbf{u}_{12}^*$, which is of the same length as $\mathbf{u}_1^*$, perpendicular to $\mathbf{u}_3^*$ and making an angle ϕ against $\mathbf{u}_1^*$ is introduced. The components s_e and s_m of a reciprocal vector $\mathbf{s}$ is defined as:

$$\mathbf{s}=s_e\mathbf{u}_{12}^*+s_m\mathbf{u}_3^*=\frac{s_e}{\sin\gamma|\mathbf{u}_1|}\frac{\mathbf{u}_{12}^*}{|\mathbf{u}_{12}^*|}+\frac{s_m}{|\mathbf{u}_3|}\frac{\mathbf{u}_3^*}{|\mathbf{u}_3^*|} \tag{38}$$

The scattering intensity of the irradiated volume can be calculated as:

$$I_s(s_e,s_m)=\frac{N_b}{2\pi}\int_0^{2\pi}I_b(s_1,s_2,s_3)\mathrm{d}\phi \tag{39}$$

$$s_1=\frac{\sin(\phi+\gamma)}{\sin\gamma}s_e \tag{40}$$

$$s_2=\frac{\sin\phi}{\sin\gamma}s_e \tag{41}$$

$$s_3=s_m \tag{42}$$

2.7. Determination of structure parameters

The scattering intensity can be calculated from the values of the structure parameters using the equations so far derived. In the following, the equations for determining size parameters from the scattering intensity distributions are considered based on Eqs. (4), (13), (36) and (38)–(42). All the assumptions made for deriving these equations are adopted. In addition, it is assumed that R_j and ζ_j are constant around each scattering peak and $N_1=N_2$. As shown in Fig. 2, the peak positions of the meridional scattering measured as a function of 2θ, $|\mathbf{s}|$ and s_m along the line S–T are denoted as $2\theta_p$, $|\mathbf{s}|_p$ and s_{mp}, respectively. The FWHM's of the meridional scattering measured as a function of 2θ, $|\mathbf{s}|$ and s_e along the line U–V are denoted as $\Delta(2\theta)$, $\Delta|\mathbf{s}|$ and Δs_e, respectively.

The height of the unit cell $|\mathbf{u}_3|$ can be determined from $2\theta_p$. When the variation of $|F(\rho_u)|^2$ with s_3 is much smaller than the variation of $G(N_3, R_3, \zeta_3, s_3)$, the intensity distribution as a function of s_m is determined by $G(N_3, R_3, \zeta_3, s_3)$ which produces the peaks of order h_3 at $s_{mp}=h_3+\zeta_3$. Therefore, the Bragg equation can be modified as follows.

$$|\mathbf{u}_3|=\frac{h_3+\varsigma_3}{|\mathbf{s}|_p}=\frac{(h_3+\varsigma_3)\lambda}{2\sin\theta_p} \tag{43}$$

It should be noted the when $\zeta_3=1/2$, the meridional scattering closest to the center beam is so to speak the 0.5th order scattering ($h_3=0$, $h_3+\zeta_3=0.5$). The height of the unit cell determined with the Bragg equation from this scattering by misidentifying it as the 1st order scattering is twice the true value.

The length of the rod $N_3|\mathbf{u}_3|$ and the degree of disorder R_3 influence the FWHM of the intensity distribution in parallel to the meridian through $G(N_3, R_3, \zeta_3, s_3)$. If the values of FWHM for the scatterings with several different orders are available, $N_3|\mathbf{u}_3|$ and R_3 can be determined individually using the Hosemann equation [11]. If the scattering is too broad to apply the Hosemann equation, the degree of disorder can be estimated by a method proposed in a previous paper [13].

The transverse size of the bundle $N_1|\mathbf{u}_1|$ is determined from $\Delta(2\theta)$ provided that the disorder is small. When the disorder is so small that $R_1=R_2=1$ and $\zeta_1=\zeta_2=0$, $G(N_1, R_1, \zeta_1, s_1)G(N_2, R_2, \zeta_2, s_2)$ is an exponential function of $-\pi N_1^2(s_1^2+s_2^2)$. The average of $-\pi N_1^2(s_1^2+s_2^2)$ with respect to ϕ is $-\pi N_1^2(s_e/\sin\gamma)^2$. On the other hand, $|F(\rho_u)|^2$ is an exponential function of $-0.2653Q^2=-0.2653(\pi\alpha_1)^2(s_e/\sin\gamma)^2$ which is smaller than $-\pi N_1^2(s_e/\sin\gamma)^2$. Hence, $G(N_1, R_1, \zeta_1, s_1)G(N_2, R_2, \zeta_2, s_2)$ shows a larger variation with s_e than $|F(\rho_u)|^2$ does and determines the intensity distribution as a function of s_e. Therefore, the following Scherrer equation is available.

$$N_1|\mathbf{u}_1|=2\left(\frac{\ln 2}{\pi}\right)^{1/2}\frac{|\mathbf{u}_1|\sin\gamma}{\Delta s_e}=2\left(\frac{\ln 2}{\pi}\right)^{1/2}\frac{1}{\Delta|\mathbf{s}|}$$
$$=2\left(\frac{\ln 2}{\pi}\right)^{1/2}\frac{\lambda}{\Delta(2\theta)}=\frac{0.94\lambda}{\Delta(2\theta)} \tag{44}$$

The unit cell diameter $\alpha_1|\mathbf{u}_1|$ is determined from $\Delta(2\theta)$ provided that the disorder is large. When the disorder is so large that $R_1=R_2=0$, $G(N_1, R_1, \zeta_1, s_1)G(N_2, R_2, \zeta_2, s_2)$ does not depend on s_1 and s_2. In this case, $|F(\rho_u)|^2$ determines the intensity distribution as a function of s_e. Therefore, the following equation can be derived.

$$\alpha_1|\mathbf{u}_1|=\frac{2}{\pi}\left(\frac{\ln 2}{0.27}\right)^{1/2}\frac{|\mathbf{u}_1|\sin\gamma}{\Delta s_e}=\frac{2}{\pi}\left(\frac{\ln 2}{0.27}\right)^{1/2}\frac{1}{\Delta|\mathbf{s}|}$$
$$=\frac{2}{\pi}\left(\frac{\ln 2}{0.27}\right)^{1/2}\frac{\lambda}{\Delta(2\theta)}=\frac{1.0\lambda}{\Delta(2\theta)} \tag{45}$$

The influence of the change in the packing density of the rods in the bundle can be predicted based on Eqs. (44) and (45). The compaction of the packing of the rods corresponds to the decrease in $|\mathbf{u}_1|$ by keeping constant values of $\alpha_1|\mathbf{u}_1|$ and N_1. Eqs. (44) and (45) predict that the compaction leads to the increase in $\Delta(2\theta)$ when the disorder is small but it does not influence $\Delta(2\theta)$ when the disorder is large.

3. Calculation of scattering patterns

3.1. Conditions of calculation

The scattering patterns of the fibers consisting of the bundles of long-period structures were calculated based on the equations so far derived by assuming that incident X-ray beam was perpendicular to the fiber axis. The conditions and the values of the structure parameters used for calculation are shown in Tables 2 and 3. Among the structure models F01 to F16, F11 represents a series of structures, which vary in ω_{13}

Table 2
Conditions used for calculating scattering patterns

Items	Conditions (equations)
I_e, ρ_d, v, N_b	Arbitrary constants
Lattice vectors	$\|\mathbf{u}_1\|=\|\mathbf{u}_2\|$
	Angle between $\mathbf{u}_1$ and $\mathbf{u}_3$ is $\pi/2$
	Angle between $\mathbf{u}_2$ and $\mathbf{u}_3$ is $\pi/2$
	Angle between $\mathbf{u}_1$ and $\mathbf{u}_2$ is $\pi/3$
Unit cell	Columnar (Eq. (36))
	$\alpha_1=\alpha_2$
Size of lattice	$N_1=N_2$
Disorder of lattice	Three-dimensionally propagating disorder (Eq. (13))
	Rectangular distribution (Eq. (29))
	$D_1(\mathbf{x})=D_2(\mathbf{x})$
	$\omega_{11}=\omega_{12}=\omega_{21}=\omega_{22}$
	$\omega_{13}=\omega_{23}$
	$\omega_{31}=\omega_{32}$
Orientation of bundles	Unidirectional and cylindrically symmetric (Eq. (39))
Incident X-ray beam	Perpendicular to fiber axis

and the values of ω_{13} are indicated by the figures after F11 as F11-ω_{13}. The calculated intensities were normalized by the intensity at $(s_e, s_m)=(0, 0)$ for each structure model. The scattering patterns were obtained by converting the scattering intensities to the brightness levels using the conversion rates which were constant for F01 to F09 and slightly varied for F10 to F16 so the features of the scattering patterns might be easily grasped. As shown in Fig. 2, the s_e and the s_m axis were taken in the horizontal and the vertical direction, respectively. The displayed region of the patterns is also shown in Fig. 2. Since the Ewald sphere can be approximated by a plane for the small-angle scattering, the calculated intensity distributions on the s_e-s_m plane are comparable with the measured scattering patterns where the magnitude of the scattering vectors in the equatorial and meridional directions is given by $s_e/(\sin\gamma\ |\mathbf{u}_1|)$ and $s_m/|\mathbf{u}_3|$ according to Eq. (38).

3.2. Influences of structure parameters on scattering patterns

Each of F02 to F09 differs from a reference structure model F01 in a certain structural feature and the calculated patterns of F01 to F09 are shown in Fig. 5. By comparing the calculated patterns of F02 to F09 with that of F01 and referring to Eq. (13), the following remarks can be made with respect to the influences of the structure parameters on the appearance of the scattering patterns.

3.2.1. Unit cell sizes, α_1, α_2 and α_3

The larger α_j is, the more rapidly $|F(\rho_u)|^2$ decreases with increasing s_j. When α_1 $(=\alpha_2)$ increases, the scattering spots of higher orders h_1 and h_2 disappear (F02). When α_3 increases, the scattering spots of higher order h_3 disappear (F03).

3.2.2. Lattice sizes, N_1, N_2 and N_3

The larger N_j is, the sharper peaks $G(N_j, R_k, \zeta_k, s_j)$ produces as a function of s_j. When N_1 $(=N_2)$ increases, the scattering spots shrink in the equatorial direction (F04). When N_3 increases, the scattering spots shrink in the meridional direction (F05).

3.2.3. Disorder between longitudinally adjacent unit cells, ω_{31}, ω_{32} and ω_{33}

The increase in ω_{31}, ω_{32} and ω_{33} decreases R_3 and hence the peak height of $G(N_3, R_3, \zeta_3, s_3)$ but increases the baseline height of this function (Appendix A). As a result, the scattering spots turn into the streaks parallel to the meridian. For a large ω_{31} $(=\omega_{32})$, R_3 decreases markedly with increasing s_e and the scattering spots of higher orders h_1 and h_2 turn into the streaks parallel to the meridian (F06). For a large ω_{33}, on the other hand, R_3 decreases markedly with increasing s_m and the scattering spots of higher order h_3 turn into the streaks parallel to the meridian (F07).

Table 3
Values of structure parameters used for calculating scattering patterns

Structure model	α_1	α_3	N_1	N_3	ω_{11}	ω_{13}	ω_{31}	ω_{33}
F01	0.5	0.3	3	4	0	0	0	0
F02	1.0	0.3	3	4	0	0	0	0
F03	0.5	0.9	3	4	0	0	0	0
F04	0.5	0.3	6	4	0	0	0	0
F05	0.5	0.3	3	8	0	0	0	0
F06	0.5	0.3	3	4	0	0	1.0	0
F07	0.5	0.3	3	4	0	0	0	1.0
F08	0.5	0.3	3	4	1.0	0	0	0
F09	0.5	0.3	3	4	0	1.0	0	0
F10	1.0	0.4	1	4	0	0	0	1.2
F11-ω_{13}	1.0	0.3	3	4	0	ω_{13}	0	0.4
F12	1.0	0.4	4	4	0	1.2	0	0.4
F13	1.0	0.4	4	4	0	1.6	0	0.4
F14	1.0	0.4	4	4	0	0.6	0	1.2
F15	1.0	0.4	4	4	0	1.0	0	1.2
F16	0.4	0.2	2	4	1.0	1.0	0	1.6

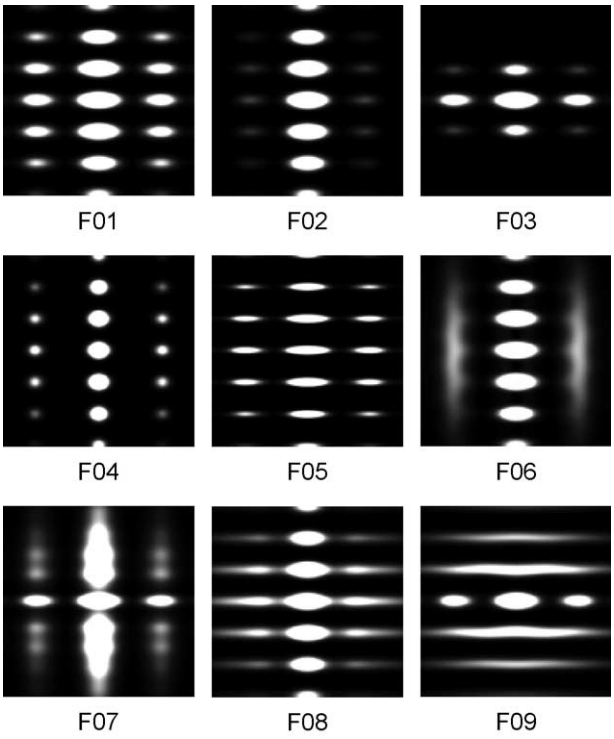

Fig. 5. Calculated scattering patterns of F01 to F09.

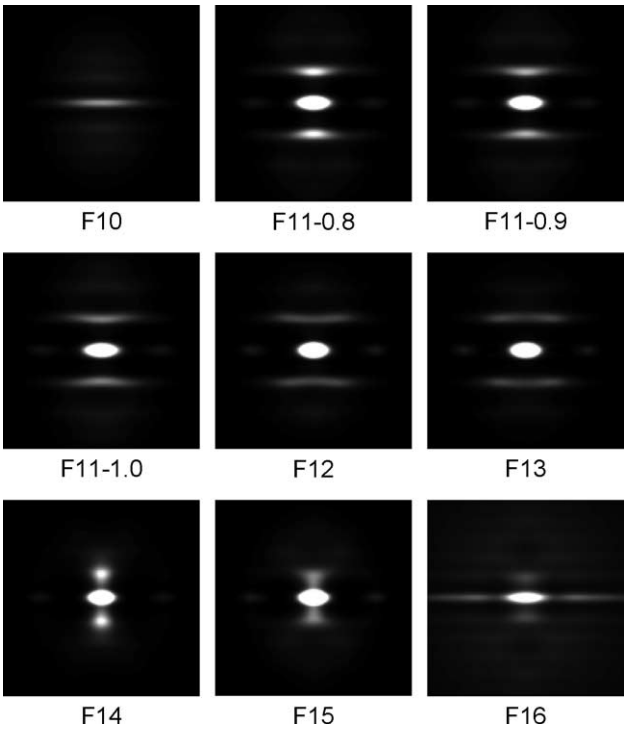

Fig. 6. Calculated scattering patterns of F10 to F16.

3.2.4. Disorder between transversely adjacent unit cells, ω_{11}, ω_{12}, ω_{13}, ω_{21}, ω_{22} and ω_{23}

The increase in ω_{11}, ω_{12}, ω_{13}, ω_{21}, ω_{22} and ω_{23} decreases R_1 and R_2 and hence the peak height of $G(N_1, R_1, \zeta_1, s_1)G(N_2, R_2, \zeta_2, s_2)$ but increases the baseline height of this function (Appendix A). As a result, the scattering spots turn into the streaks parallel to the equator. For a large ω_{11} ($=\omega_{12}=\omega_{21}=\omega_{22}$), R_1 and R_2 decrease markedly with increasing s_e and the scattering spots of higher orders h_1 and h_2 turn into the streaks parallel to the equator (F08). For a large ω_{13} ($=\omega_{23}$), on the other hand, R_1 and R_2 decrease markedly with increasing s_m and the scattering spots of higher order h_3 turn into the streaks parallel to the equator (F09).

3.3. Characteristic scattering patterns of polymers

The structure parameters of F10 to F16 were chosen so that they produce characteristic scattering patterns often observed with polymers. The calculated patterns of F10 to F16 are shown in Fig. 6. The following remarks can be made with respect to the features of the scattering patterns and the structures.

3.3.1. Equatorial streak

When the rods are isolated from each other so that there is no interference of X-rays, the bundle can be regarded as consisting of a single rod. When ω_{33} is small as well, several streaks in parallel to the equator are produced. When ω_{33} is large, on the other hand, the equatorial streak is produced alone (F10). When the rods form a bundle whereas the distortion between the rods ω_{11} ($=\omega_{12}=\omega_{21}=\omega_{22}$) and ω_{33} are large, the equatorial streak having a maximum or a shoulder is produced alone.

3.3.2. Layer line and four-spot scattering

The calculated patterns of F11 with various values of ω_{13} demonstrate the significant influences of this parameter on the appearance of the scattering pattern. With increasing ω_{13} ($=\omega_{23}$) up to 1, the meridional scattering is elongated in parallel to the equator and the layer line scattering is developed (F11-0.8, 0.9 and 1.0). Due to a large α_1 of this structure, the first order equatorial scattering spots, which are clearly observed for F09 are weak. When ω_{13} increases beyond 1, the four-spot scattering which has maxima at $s_e=1/2$ instead of $s_e=0$ is developed. The four-spot scattering is developed since $R_j\exp(2\pi i\zeta_j)$ takes a negative value and hence $\zeta_j=1/2$ at $s_m=1$ ($j=1$ and 2). In general, $R_j\exp(2\pi i\zeta_j)$ in Eq. (29) takes a negative value for $1<\omega_{j3}<2$ at $s_3=1$ if $\omega_{j1}=\omega_{j2}=0$. It should be noted that the structure causing the four-spot scattering does not have the periodicity directly related to the scattering maxima. Slight concave and convex bendings from the straight layer line are observed for F12 and F13.

Fig. 7 shows the calculated intensity distributions along the line U–V shown in Fig. 2 at $s_m=1$ for F11. The characteristic feature of the change of the intensity distribution is that with decreasing ω_{13} the intensity increases preferentially in the center of the layer line without causing large change in the tails. This feature resembles that found in Fig. 1.

Fig. 8 shows the relation between ω_{13} and Δs_e for the intensity distributions shown in Fig. 7. The value of Δs_e for F11 predicted from Eq. (44) is 0.27, which is in accordance with the value at $\omega_{13}=0$ shown in Fig. 8. The value of Δs_e for F11 predicted from Eq. (45) is 0.88, which is in accordance with

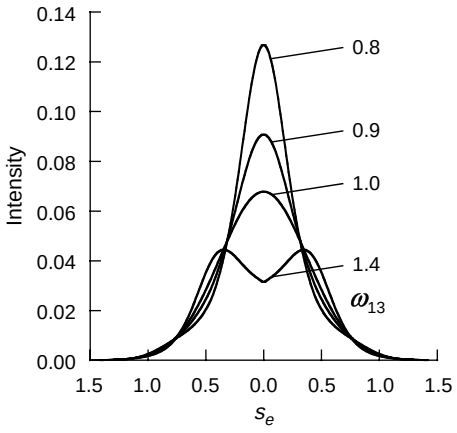

Fig. 7. Calculated intensity distributions of the meridional scattering along the line U–V shown in Fig. 2 at $s_m=1$. Calculation was based on F11 with various values of ω_{13} shown in the figure.

the value at $\omega_{13}=2$ shown in Fig. 8. For the values of ω_{13} between 1 and 2, Δs_e takes a larger value than the prediction of Eq. (45) due to the development of the four-spot scattering.

3.3.3. Droplet-shaped and triangular scattering

When ω_{33} is very large, $R_3\exp(2\pi i\zeta_3)$ takes a negative value and $\zeta_3=1/2$ in a certain region of s_m. This displaces the scattering spot from $(s_e, s_m)=(0, 1)$ to (0, 1/2). As shown above, the scattering spot is elongated in parallel to the equator with increasing ω_{13} $(=\omega_{23})$. As a result, the droplet-shaped scattering is produced when ω_{33} is large and ω_{13} takes a moderate value (F14). The triangular scattering with its apex on the center of the scattering pattern is produced when ω_{33} and ω_{13} are large (F15). It should be noted that these structures do not have the periodicity directly related to the scattering maxima. When ω_{11} $(=\omega_{12}=\omega_{21}=\omega_{22})$ is large as well, the scattering spots on the equator are elongated in parallel to the equator. Thus the equatorial streak is produced in addition to the triangular scattering (F16). It should be noted that the equatorial streak and the triangular scattering of this pattern are not produced by different components of the fiber structure but the bundle of long-period structures produces both of these scatterings simultaneously.

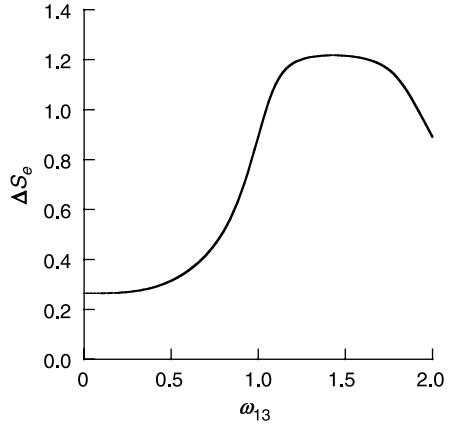

Fig. 8. Plot of Δs_e versus ω_{13} for F11.

3.3.4. Other type of scattering

The cross-shaped scattering will be obtained if it is assumed that $\mathbf{u}_1$ and/or $\mathbf{u}_2$ are not perpendicular to $\mathbf{u}_3$. The scattering patterns of the interlocking shish–kebab structure [4] and a structure in which transversely neighbouring crystalline regions are shifted stepwise [14] will be calculated if it is assumed that $\mathbf{u}_1$ is not perpendicular to $\mathbf{u}_3$ and β_3 in Eq. (35) takes a value which makes the bases of the crystalline regions perpendicular to $\mathbf{u}_3$.

3.3.5. Higher order scattering

In the calculated patterns of Fig. 6, a trace of higher order scattering is discernible in addition to the main scatterings mentioned above. In the actual measurements, the higher order scatterings are reduced due to several factors, which have not been taken into account in the present calculation. These factors are, for example, the fluctuation of the electron density in the unit cell [8], the distributions in the shapes and the sizes [8] of the unit cells, the orientation distributions of the unit cells and the rods, and the threshold level of the detector below which no X-ray can be detected even with the measurements for a long duration.

3.4. Scattering patterns of PET fiber

SAXS of the PET fiber shown in Fig. 1 was analyzed based on the model consisting of the bundles of long-period structures. The structure parameters were determined by comparing the calculated and the measured intensity distributions. The conditions shown in Table 2 were used for calculation.

Since α_1 is expected to be large from the absence of the first order equatorial scattering spot, α_1 was assumed to be 1. This means that the rods are closely packed in the bundle and the values allowed for ω_{11} and ω_{31} are 0. The value of $|\mathbf{u}_3|$ was estimated to be about 14 nm by applying Eq. (43) with $h_3+\zeta_3=1$ to the measured value of $|\mathbf{s}|_p$. On the other hand, the size of the crystalline region in parallel to the fiber axis $\alpha_3|\mathbf{u}_3|$ was estimated to be about 4.2 nm by applying the Scherrer equation to the $\bar{1}05$ peak of the wide-angle X-ray diffraction (WAXD) of this fiber. Therefore, α_3 was determined to be 0.3. The values of N_1, N_3 and ω_{33} were determined so that the calculated patterns did not bend largely from the layer line and showed the meridional peak width close to the measured values. The values of $\sin\gamma\ |\mathbf{u}_1|$ and ω_{13} were determined by a trial-and-error method so that the calculated intensity distributions at a constant s_m of the intensity maximum fitted to the measured intensity distributions shown in Fig. 1. The structure parameters determined in this way have been adopted for F11 in Table 3. The values of $\sin\gamma\ |\mathbf{u}_1|$, $|\mathbf{u}_3|$ and ω_{13} are shown in Table 1 and Fig. 9. The sizes of the crystalline region perpendicular to the fiber axis were determined to be 4.3 and 5.5 nm by applying the Scherrer equation to the 100 and the 010 peak of WAXD of this fiber, respectively. The unit cell diameter $\alpha_1|\mathbf{u}_1|$ was calculated to be 6 nm from the values of $\sin\gamma\ |\mathbf{u}_1|$ shown in Table 1. This value is considered to be a reasonable one in comparison with the crystallite sizes.

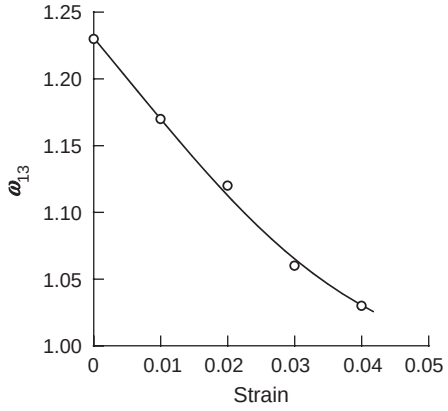

Fig. 9. Plot of ω_{13} versus strain of a PET fiber. The values of ω_{13} were determined by fitting the calculated intensity distribution based on F11 to the measured intensity distributions shown in Fig. 1.

The solid lines in Fig. 1 show the calculated intensity distributions of F11 with the values of the structure parameters shown in Tables 1 and 3 and Fig. 9. The calculated intensity distributions well represent the measured changes of the intensity distribution of the PET fiber caused by tensile deformation. Therefore, the change of the scattering pattern from the four-spot to the layer line scattering can be attributed to the slight decrease in ω_{13}. One possible interpretation of the decrease in ω_{13} with tensile deformation is schematically illustrated in Fig. 10. This figure shows that the long-period structures are initially arranged with a large distribution of the vectors joining transversely neighbouring crystalline regions. By the tensile deformation of the fiber, the long-period structures are mutually slipped along the fiber axis as shown by the arrows in the figure until the neighbouring crystalline regions come in contact. As a result, the distribution of the vectors is reduced and ω_{13} is decreased. Although the increase in $|\mathbf{u}_3|$ with the fiber strain up to 0.04 was not so large in Table 1, $|\mathbf{u}_3|$ increased substantially when much larger strain was applied to the fiber. The details will be shown in a succeeding paper.

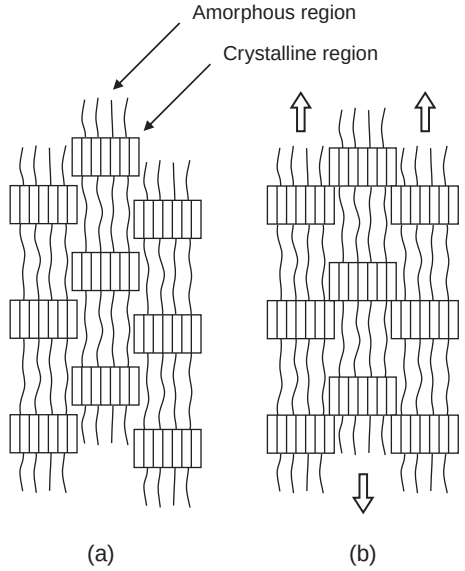

Fig. 10. Schematic illustrations of the bundle of long-period structures (a) before and (b) after the long-period structures are slipped in the direction of the arrows by the tensile deformation of the fiber.

The appearance of the scattering pattern changes sensitively depending on ω_{13}. This means that the functional form of D_j also has significant influences. More complete fitting of the calculated and the measured scattering patterns will be obtained if the functional form will be refined. It should be kept in mind that the model proposed in this study is not the only one, which accounts for the measured scattering patterns of the PET fiber since there are different structures, which give the same scattering pattern.

4. Conclusions

The small-angle scattering patterns were calculated based on a structure model, which consisted of the bundles of long-period structures. The equations for determining the structure parameters from the scattering intensity distributions were also derived. The proposed model produced various scattering patterns of polymers, such as the equatorial, layer line, four-spot, droplet-shaped and triangular scattering. The disorder in and between the long-period structures had significant influences on the appearance of the scattering patterns. The 0.5th order scattering arose when the disorder was large even though the structure did not have the periodicity directly related to the intensity maximum. A slight decrease in the disorder due to slip between the long-period structures accounted for the sudden change of the SAXS pattern of a PET fiber from the four-spot to the layer-line scattering which was caused by a slight tensile deformation.

Acknowledgements

This work was supported by High-strength Fiber Project, Technology for Precisely Controlled Polymers, Nano-technology Program for Materials Development promoted by New Energy and Industrial Technology Development Organization, Japan. The measurements of SAXS have been performed at BL15A of Photon Factory, High Energy Accelerator Research Organization, Japan under the approval of the Photon Factory Program Advisory Committee (proposal no. 2004G311).

Appendix A

Eqs. (14) and (27) can be derived as follows. In this study, the value of R_j^0 at $R_j=0$ is defined to be 1. It is assumed that R_j and ζ_j are constant around each scattering peak.

In the case of $0 \le R_j < 1$, the summation of series in Eq. (14) can be calculated as follows.

$$\sum_{n=-\infty}^{\infty} R_j^{|n|} \exp(2\pi n i[s_j - \varsigma_j]) = \frac{1-R_j^2}{1+R_j^2-2R_j\cos(2\pi[s_j-\varsigma_j])} \tag{A1}$$

The function in the right side of this equation takes a maximum value of $(1+R_j)/(1-R_j)$ at $s_j-\zeta_j=h_j$ and a minimum value of $(1-R_j)/(1+R_j)$ at $s_j-\zeta_j=h_j+(1/2)$. If this function is separated into a baseline with a height of $(1-R_j)/(1+R_j)$ and a peak function with a peak height of $4R_j/(1+R_j^2)$, the area of the peak function between $s_j-\zeta_j=h_j-(1/2)$ and $h_j+(1/2)$ is calculated to be $2R_j/(1+R_j)$. This peak function is approximated by an exponential function, which has the same height and area as the original peak function where the area of the exponential function is calculated over infinite range of $s_j-\zeta_j$. The approximate function found in this way takes the following form.

$$\sum_{n=-\infty}^{\infty} R_J^{|n|}\exp(2\pi ni[s_j-\varsigma_j]) \approx \frac{4R_j}{1-R_j^2}\exp\left(-4\pi\left[\frac{s_j-\varsigma_j-h_j}{1-R_j}\right]^2\right)+\frac{1-R_j}{1+R_j} \tag{A2}$$

This equation also represents the case of $R_j=1$ as the limiting value. The Fourier transform of Z_j with respect to x_j can be calculated as:

$$F(Z_j(x_j)) = N_j^2\frac{\sin^2(\pi N_j s_j)}{(\pi N_j s_j)^2} \approx N_j^2\exp\left(-\pi N_j^2 s_j^2\right) \tag{A3}$$

The convolution product of the functions in the right side of Eqs. (A2) and (A3) with respect to s_j can be calculated by applying the relation

$$\exp\left(-As_j^2\right)^*\exp(-B[s_j-\varsigma_j]^2) = \left(\frac{\pi}{A+B}\right)^{1/2}\exp\left(-\frac{AB}{A+B}[s_j-\varsigma_j]^2\right) \tag{A4}$$

where $A+B\geq 0$. The result of calculation has been shown in Eq. (14). Eq. (27) can be derived for $0\leq R_j<1$. This equation also represents the case of $R_j=1$ as the limiting value.

References

[1] Shimizu J, Okui N, Kikutani T. Sen'i Gakkaishi 1981;37(4):T135–T42.
[2] Shimizu J, Kikutani T, Takaku A, Okui N. Sen'i Gakkaishi 1981;40(2): T63–T71.
[3] Fujimoto K, Iohara K, Ohwaki S, Murase Y. J Appl Polym Sci 1991;42: 1509–17.
[4] Funai E, Sakurai S, Hara S, Yamamoto K, Okamoto S, Kojima J, et al. Sen'i Gakkaishi 2004;60:322–30.
[5] Fischer EW, Fakirov S. J Mater Sci 1976;11:1041–65.
[6] Stockfleth J, Salamon L, Hinrichsen G. Colloid Polym Sci 1993;271: 423–35.
[7] Tsvankin DY. Polym Sci USSR 1964;6(11):2304–9.
[8] Tsvankin DY. Polym Sci USSR 1964;6(11):2310–8.
[9] Gerasimov VI, Tsvankin DY. Polym Sci USSR 1969;11(12):3013–32.
[10] Gerasimov VI, Zanegin VD, Tsvankin DY. Polym Sci USSR 1979;20(2): 954–62.
[11] Bonart R, Hosemann R, McCullough R. Polymer 1963;4:199–211.
[12] Shioya M, Takaku A. Acta Crystallogr 1988;A44:150–7.
[13] Shioya M, Takaku A. J Polym Sci, Part B 1993;31:1519–28.
[14] Bonart R, Hosemann R. Kolloid ZZ Polym 1962;186:16–29.